INTERNATIONAL JOURNAL FOR NUMERICAL METHODS IN FLUIDS
Int. J. Numer. Meth. Fluids 2000; **33**: 961–992

Simulation of coating flows with slip effects

V. Ngamaramvaranggul and M. F. Webster*

Institute of Non-Newtonian Fluid Mechanics, Department of Computer Science, University of Wales, Swansea, U.K.

SUMMARY

This work is concerned with the numerical prediction of wire coating flows. Both annular tube-tooling and pressure-tooling type extrusion–drag flows are investigated for viscous fluids. The effects of slip at die walls are analysed and free surfaces are computed. Flow conditions around the die exit are considered, contrasting imposition of no-slip and various instances of slip models for die wall conditions. Numerical solutions are computed by means of a time marching Taylor–Galerkin/pressure–correction finite element scheme, that demonstrates how slip conditions on die walls mitigate stress singularities at the die exit. For pressure-tooling and with appropriate handling of slip, reduction in shear rate at the die exit may be achieved. Maximum shear rates for tube-tooling are about one quarter of those encountered in pressure-tooling. Equivalently, extension rates peak at land entry, and tube-tooling values are one third of those observed for pressure-tooling. With slip and tube-tooling, peak shear values at die exit may be almost completely eliminated. Nevertheless, in contrast to the pressure-tooling scenario, this produces larger peak shear rates upstream within the land region than would otherwise be the case for no-slip.

KEY WORDS: free surface; pressure-tooling; slip effect; tube-tooling; wire coating flow

1. INTRODUCTION

This paper documents the application of a time marching (semi-implicit) Taylor–Galerkin/pressure–correction finite element scheme (STGFEM) [1,2] to solve annular incompressible coating flows for Newtonian fluids, associated with coatings of wire and cable, fibre-optic cables or glass rovings. Unique aspects of this work include the specific treatment of free surfaces and the incorporation of slip conditions. This study is conducted with the aim of providing a deeper understanding of the design of coating processes, through a comparative study of both pressure-tooling and tube-tooling type flow situations. Emphasis is placed upon the analysis of flow conditions around the die exit: particularly so on shear and strain rates, and identification of the influence of slip. In such a fashion, a long-term goal is to improve the understanding of process performance and hence for this to ultimately impact upon product optimization.

* Correspondence to: Institute of Non-Newtonian Fluid Mechanics, Department of Computer Science, University of Wales, Singleton Park, Swansea, SA2 8PP, U.K.

Received May 1999
Revised September 1999

The wire coating process [3–5] plays an important role in the modern industrial processing. This process involves the extension of a molten polymer over a moving wire, and typically requires a wire preheater, an extruder with a cross-head shaped die, a cooling trough for the extruded wire, and a take-up and payoff device. There are two main types of annular extrusion coating designs: namely tube-tooling, used for wide-bore coatings, and pressure-tooling, associated with narrow gauge wires, see Han and Rao [6]. For the case of pressure-tooling, the molten polymer meets the moving wire under pressure within the die. For tube-tooling, the die design is slightly different in shape. Here, the molten polymer and wire move parallel to one another as they pass through the die without contact. On departing the die, the polymer is drawn down onto the wire by virtue of the additional drag flow component induced by the motion of the wire. Since contact between polymer and wire occurs beyond the die for tube-tooling, the shape of the extrudate is of considerable importance. Control of this external coating flow can provide improved smoothness of the polymer coating to the wire/cable, guaranteeing integrity of the surface, which in turn may satisfy quality assurance measures on mechanical and insulation properties.

The majority of mathematical studies for coating extrusion have concentrated on high-speed pressure-tooling, whilst comparatively little attention has been devoted to coating flows in tube-tooling dies. A number of simplifying assumptions are customary. For example, the process may be taken as isothermal, the fluid rheology of the coating material as viscous (typically inelastic), and the flow analysed under a lubrication approximation (see, for example, References [5–8]). Short die channels are often taken that influence imposed entry and exit conditions [9]. Our approach in this study is to take isothermal viscous assumptions and to treat the flow as incompressible and concentric.

Let us first consider pressure-tooling. Kasayima and Ito [10] theoretically analysed the drag flow corresponding to the external flow from a pressure-tooling die by considering many small cross-sections to this flow. Each section was analysed separately, assuming constant axial velocity and viscosity on each section. This amounts to a semi one-dimensional analysis. Using Newtonian and power-law inelastic modelling, they derived expressions for shear, axial velocity and flow rate.

Significant interest has been focused on the internal polymer flow within the die, such as for pressure-tooling flows, as analysed theoretically by Paton *et al.* [11] and McKelvey [12] for Newtonian and power-law fluids. These authors approximated the flow by considering drag flow and pressure-driven flow separately, and expressions were obtained for shear rate, flow rate and the radial velocity distribution. When the radius of the die is almost that of the wire, the annulus can be approximated by a thin parallel slit. Paton *et al.* demonstrated that the corresponding error under such an approximation is negligible for pressure-driven flow, though this may be quite considerable for drag flow.

The case of a complete pressure-tooling flow has been analysed by Mitsoulis *et al.* [5] and Caswell and Tanner [8]. Caswell and Tanner [8] proposed a new die design to pressure-tooling with a blunted guider nose tip, which eliminated fluid recirculation at the contact point of the guider nose tip and wire. For the instance of tube-tooling, a full flow specification with both die and extrudate flow is considered in Mutlu *et al.* [7]. We follow this work in adopting again a fixed melt–cable contact point, as this has already proven to be an acceptable assumption.

A number of papers on experimental studies have appeared, investigating the stability of the die extrudate, see, for example, those by Hatzikiriakos and Dealy [13] and Ramamurthy [14]. Slip at and around the die exit plays an important role in the behaviour of the extrudate flow, as discussed by Sillilman and Scriven [15]. In the Hatzikiriakos and Dealy article, flowrate (Q) and pressure (P) changes were investigated separately, as to the influence exhibited on linear polymer high density polyethylene (HDPE). These authors calculated the slip velocity along the solid boundary surface as a function of wall shear stress, and investigated its contributive role to oscillations on the surface of the fluid extrudate. This work of Ramamurthy focussed on polyethylenes at low deformation rate and corresponding extrudate irregularities, more commonly known as melt fracture. Ramamurthy suggested that the surface melt fracture phenomenon is localized to the die exit region. This is attributed to the large local stresses that arise and critically depends upon the breakdown of adhesion at the point of separation of the polymer melt with the die. Based upon this realization, a power-law interpretation has emerged for wall slip. Melt fracture may arise in two forms of classification; namely surface or gross irregularities. The former, occurring under steady flow conditions, can range from slight disturbance to the sharkskin effect. This corresponds primarily to the breakdown of adhesion, resulting in a finite fluid (slip) velocity at the die wall. The second melt fracture type, manifested as gross irregularities, can range from mild helical to random distortions of the extrudate melt. Principally, we are concerned here with the influences that may bring about the former surface irregularities.

Numerical solutions involving slip have been documented by Silliman and Scriven [15] for Newtonian fluids and Phan-Thien [16] for visoelastic fluids. Both these studies targeted imposition of slip in a steady two-dimensional, planar extrusion flow scenario, with a fixed flow rate and a sharp slot edge to the die exit. This may depart from experimental practice, when a fixed pressure drop may be imposed across the flow (as opposed to a fixed flow rate), which generates transient variations with slip (intrinsically unsteady), see Hatzikiriakos and Dealy [13]. A dynamic approach has been adopted in a most recent study by Den Doelder *et al*. [17], where they compare the wall slip and the constitutive approach for modelling spurt instabilities in polymer melt flows. Phan-Thien studied the influences of slip via a time marching boundary element method (BEM) as an iterative procedure, satisfying a steady slip velocity condition. This led to a dependency on wall shear stress, which must surpass some critical value to trigger slip, based on the experimental data and ideas proposed in Ramamurthy [14]. In such a manner, planar viscoelastic flows were analysed employing an exponential Phan Thien/Tanner (PTT) model. This provides some insight as to how the level of critical wall shear stress influences the onset of slip within the die, the magnitude of slip velocities that result and the shape of the consequent swelling. In contrast, Silliman and Scriven [15] introduced slip conditions via the Navier slip law, using the naturally occurring stress-related boundary terms that arise in a weak-form weighted-residual Galerkin variational formulation implemented through a finite element method (FEM). For Newtonian fluids, this study of wall-slip revealed that raising the Reynolds number decreases the die swell, and reduces the influence of the die exit on the jet flow velocity profile. Hence, it is observed that slip trends to have a straightening out effect upon the free-jet surface profile, as does the action of surface tension similarly.

In a series of articles, we have documented the use of STGFEM formulation for the numerical prediction of wire-coating flows. In all such studies, no-slip conditions were assumed within the die. Inelastic modelling was used by Binding *et al.* [18] to predict the shear and extensional flow behaviour of low density polyethylene (LDPE) melts associated with a pressure-tooling flow. There, various viscous models were compared with reference to stress and pressure fields generated, ranging from pure shear to pure extensional, with combinations in between. The influence of short residence times of polymer particles within the die was recongnized and a viscoelastic analysis was commended to predict residual stresses in the coatings. This subsequently led to a set of viscoelastic studies aimed at drawing flows, see Gunter *et al.* [19], which addressed benchmark extensional flows: namely a sink flow, a model draw-down flow and a conical section draw-down flow. Therein, Oldroyd-B and exponential PTT models were employed, with both coupled and decoupled schemes. For such convection-dominated flows, it was observed that numerical accuracy depended crucially on sufficient mesh refinement in the streamwise direction (with streamline upwinding). Control of cross-stream noise to the solution can be affected by increasing cross-stream mesh refinement and the number of Jacobi iterations to improve local accuracy. Such cross-stream perturbations were unaffected by streamwise numerical adjustments. Likewise, Mutlu *et al.* [7] presented solutions for a complete tube-tooling flow; a viscoelastic analysis for LDPE melts with a single-mode exponential PTT model, employing coupled and decoupled schemes. In a companion article, Mutlu *et al.* [9] studied the numerical sensitivity of solutions to stress pre-history (effect of boundary conditions) in draw-down, isolated tube-tooling, and combined tube-tooling draw-down flows. This revealed the importance of the precursor flow to deliver the appropriate inlet flow conditions to the particular flow in hand. In the most recent work of Matallah *et al.* [20] for tube-tooling flow, we have been able to perform both single-mode and multi-mode analyses, contrasting the differences in response between the use of LDPE and HDPE melts as coatings, with respect to stress, pressure and kinematic fields. These authors found stress and pressure-drop levels were doubled for HDPE over LDPE melts and pointed to the influence of the individual relaxation mode components upon residual stressing to the coating. The present work is directed towards the continuation of the above study, but concentrating upon slip and its influence on flow behaviour.

2. GOVERNING EQUATIONS

The governing equations of generalized momentum and continuity for Newtonian fluids, in the absence of body forces and incompressible isothermal flow, are expressed as

$$\rho \mathbf{U}_t = \nabla \cdot \mathbf{T} - \rho \mathbf{U} \cdot \nabla \mathbf{U} - \nabla \mathbf{p} \tag{1a}$$

$$\nabla \cdot \mathbf{U} = 0 \tag{1b}$$

$$\mathbf{T} = 2\mu \mathbf{D} \tag{1c}$$

$$\mathbf{D} = \frac{1}{2}(\nabla\mathbf{U} + \nabla\mathbf{U}^T) \tag{1d}$$

where variables velocity (**U**), pressure (**p**), extra stress tensor (**T**) and rate of deformation tensor (**D**) are defined over space and time, with temporal derivative represented as ($\mathbf{U}_t$) and matrix transpose as (^{T}). Material parameters are given via density (ρ) and viscosity (μ).

The familiar Navier–Stokes governing equations can then be derived for a constant μ. By selecting the characteristic scales of length L and velocity V, non-dimensionalization can be affected as follows:

$$\mathbf{U}^* = \frac{1}{V}\mathbf{U}, \qquad p^* = \frac{L}{\mu_0 V}p, \qquad t^* = \frac{V}{L}t$$

$$Z^* = \frac{1}{L}Z, \qquad r^* = \frac{1}{L}r, \qquad \mu^* = \frac{1}{\mu_0}\mu$$

$$\nabla^* = L\nabla, \qquad \frac{\mathrm{D}}{\mathrm{D}t^*} = \frac{L}{V}\frac{\mathrm{D}}{\mathrm{D}t}$$

where μ_0 is a reference viscosity taken here as μ. Substitution into Equations (1) renders the corresponding non-dimensional field equations

$$Re\,\mathbf{U}_t = \nabla\cdot\mathbf{T} - Re\,\mathbf{U}\cdot\nabla\mathbf{U} - \nabla p \tag{2a}$$

$$\nabla\cdot\mathbf{U} = 0 \tag{2b}$$

where $Re = \rho LV/\mu_0$, the non-dimensional group number termed the Reynolds number. Under conditions pertaining to creeping flow, Reynolds numbers are significantly less than unity, and inertial influences are minimal. This scenario is typical of polymer extrusion flows.

3. NUMERICAL SCHEME

3.1. Discretization

The Navier–Stokes equations (2) for two-dimensional, annular, incompressible, steady flow of Newtonian fluid are solved by means of a semi-implicit time stepping procedure, namely a Taylor–Galerkin/pressure–correction finite elements scheme [1,2]. These Taylor–Galerkin schemes are based on a Taylor series expansion of the solution in the time step, and use a two-step Lax–Wendroff approach to access second-order time derivatives. In this manner, a temporal discretization is affected prior to a spatial Galerkin approximation. This is largely achieved in an explicit manner via the Taylor–Galerkin procedure, though implicitness does arise through the treatment of diffusion terms. Hence, a sequence of fractional staged equations results based on operator splitting. In the first stage, a non-divergence free velocity field is computed through a predictor–corrector doublet, which invokes a half time step

calculation. The second stage involves the solution of a Poisson equation for the temporal difference of pressure. Lastly, a divergence free velocity field is computed dependent upon pressure difference. In semi-discrete form, the three fractional stages per time step are

Stage 1a

$$\frac{2Re}{\Delta t}(\mathbf{U}^{n+1/2}-\mathbf{U}^{n})=[\nabla\cdot(2\mathbf{D})-Re\,\mathbf{U}\cdot\nabla\mathbf{U}-\nabla p]^{n}+\nabla\cdot(\mathbf{D}^{n+1/2}-\mathbf{D}^{n})$$

Stage 1b

$$\frac{Re}{\Delta t}(\mathbf{U}^{*}-\mathbf{U}^{n})=[\nabla\cdot(2\mathbf{D})-\nabla p]^{n}-[Re\,\mathbf{U}\cdot\nabla\mathbf{U}]^{n+1/2}+\nabla\cdot(\mathbf{D}^{*}-\mathbf{D}^{n})$$

Stage 2

$$\frac{\Delta t}{2}\nabla^{2}(p^{n+1}-p^{n})=\nabla\mathbf{U}^{*}$$

Stage 3

$$\frac{2Re}{\Delta t}(\mathbf{U}^{n+1}-\mathbf{U}^{*})=-\nabla(p^{n+1}-p^{n})$$

where the time step index over the interval $[n, n+1]$ is denoted by n. Here, we observe the half time step $(n+1/2)$ velocity field gathered after Stage 1a and the intermediate velocity, $\mathbf{U}^{*}$, which emerges after Stage 1b.

Spatial discretization is achieved through quadratic and linear piecewise continuous interpolation on triangles for velocity and pressure respectively. Then, in conjunction with Galerkin variational weighting, the solution is computed from the above formulation based on the three fractional stages. Stages 1 and 3 are governed by mass matrices, which are solved using a Jacobi method. The pressure difference of the middle stage is solved by a direct Choleski method, relying upon the properties of the pressure matrix being symmetric and positive definite with a banded structure. The time stepping procedure is monitored for convergence to a steady state via relative increment norms (both maximum and least-squares measures) subject to satisfaction of a suitable tolerance criteria. Termination is taken in the least-squares norm.

3.2. Extrudate swell

A free surface location method is employed as a modified iterative technique by which the shape of the die extrudate is derived. For steady state Newtonian flows, a number of different alternative methods are available to determine free surface position. Three such approaches are itemized below. The first is a fixed mesh approach, involving various specific techniques to track the position of the free surface though the mesh, as suggested by Bathe [21]. The idea has some drawbacks however. The precise free surface position is not calculated, and its position

within the mesh is measured only by the mesh elements in which the free surface lies. Consequently, for reasonable accuracy, heavy refinement of the mesh is necessary, even for relatively small fluctuations in the free boundary position.

A second approach involves remeshing and a three-stage iterative cycle. This was considered by Silliman and Scriven [15] and Omodei [22]. Firstly, the free surface shape must be assumed. Next, one of the boundary conditions at the free boundary is relaxed, and the solution of the boundary value problem on the resulting domain is sought. Lastly, the previous disregarded boundary condition is used to update the shape of the free surface boundary. This process is then repeated for each iterative cycle until a predefined convergence criterion is met. A few drawbacks arise from this type of approach, the main one being the speed degradation at each iteration owing to the fact that a completely new analysis must be made for each iteration. Another disadvantage is the fixed-point type of iteration, which slows convergence and also the moderately high lack of convergence for the iterative cycle.

A third more recent approach has been used by Ruschak [23], Saito and Scriven [24], Ettouney and Brown [25], and Kistler and Scriven [26]. This technique also uses remeshing, but instead of successive iteration of the free boundary position with the field variables, the position of nodes at the free boundary is applied directly to the problem as degrees of freedom. The resulting non-linear governing equations are then solved by a Newton–Raphson iterative technique, which simultaneously calculates the free boundary position and the field variables. An advantage of using this method is a second-order rate of convergence. The main disadvantage of using this method lies in it complexity of implementation. This is due to the non-local variations with respect to the free boundary degrees of freedom, which are incorporated into the system Jacobian of the governing equations. Another disadvantage is the requirements for a refreshed system at each successive iteration.

The second approach itemized above is that favoured in the present study, for which more detail appears in [27]. An iterative process of four steps is required to compute the free surface coordinates of the extrudate swell. The first step initializes a guessed position of the free surface; the second step is to impose vanishing traction boundary conditions at the free surface, relaxing the kinematic conditions of zero flux across the surface. In this manner, a solution is computed upon the domain using the STGFEM procedure. This will generate a flow field that violates the kinematic surface condition. At a third step, this position is repaired by recomputing a new surface position, which satisfies a streamline condition for the current velocity field, emanating from the die edge. In a fourth step, a new mesh must be constructed to fit the new domain, which is achieved here by proportionally adjusting the co-ordinates of the present mesh. Steps 2–4 are then repeated successively until the kinematic condition is satisfied.

3.3. General form of boundary conditions

The general form of the boundary conditions at a solid wall may be classified into three main types as follows.

3.3.1. No-slip condition. No-slip, or stick at the wall, is a Dirichlet-type boundary condition and the velocity may be expressed there in the form

$$\hat{\mathbf{n}} \cdot U = 0, \qquad \hat{\mathbf{t}} \cdot \mathbf{U} = 0$$

where variables are defined as unit normal vector $\hat{\mathbf{n}}$, unit tangential vector $\hat{\mathbf{t}}$ and wall slip velocity vector $\mathbf{U}$.

3.3.2. Slip condition 1. This is the Navier slip law, a slip condition that is determined via tangential components alone. It provides for a combined type of Dirichlet–Robbins boundary condition

$$\alpha_0 \hat{\mathbf{t}} \cdot (\hat{\mathbf{n}} \cdot \tilde{\mathbf{T}}) - \alpha_1 \hat{\mathbf{t}} \cdot \mathbf{U} = 0, \qquad \hat{\mathbf{n}} \cdot \mathbf{U} = 0$$

The additional variables here are defined as stress tensor $\tilde{\mathbf{T}} = -p\mathbf{I} + \tau_{ij}$, pressure p, stress τ, and constant slip coefficients $\alpha_0, \alpha_1 \geq 0$.

3.3.3. Slip condition 2. Slip conditions based on normal and tangential components of traction and velocity realize the Robbins-type boundary conditions, *viz*.

$$\alpha_0 \hat{\mathbf{t}} \cdot (\hat{\mathbf{n}} \cdot \tilde{\mathbf{T}}) - \alpha_1 \hat{\mathbf{t}} \cdot \mathbf{U} = 0, \qquad \beta_0 \hat{\mathbf{n}} \cdot (\hat{\mathbf{n}} \cdot \hat{\mathbf{T}}) + \beta_1 \hat{\mathbf{n}} \cdot \mathbf{U} = 0$$

where $\beta_0, \beta_1 \geq 0$ are slip coefficients with effect to normal components, and α_0 and α_1 are as above.

It should be noted that when $\alpha_0 = \beta_0 = 0$, slip condition 2 reverts to a no-slip condition. Also, if $\beta_0 = 0$, slip condition 2 collapses to slip condition 1. Thus, slip condition 2 is the master classification, from which the other two specific instances outlined above may be extracted.

3.4. Slip velocity setting

The phenomenon of melt fracture (when the extrudate exhibits irregular behaviour) is often found to occur at low deformation levels in the polymer processing industry. The general perception of the cause of this behaviour is the influence of the critical shear stress at the die walls. The breakdown of adhesion between the polymer melt and the die wall is found to be a primary cause of surface irregularities. This breakdown is typically called 'slip', and the finite velocity generated at the die wall is termed the 'slip velocity'. The physical factors that give rise to slip are known to be both chemical and physical in nature. Ramamurthy [14] and Jiang *et al*. [28] proved from their capillary analysis that the slip velocity can be written as a function of the wall shear stress. Micro-structural flow analysis of Brunn [29], Aubert and Tirrell [30], and Goh *et al*. [31] of the slip phenomenon suggested that slip occurred due to the tendency of polymer molecules at the die wall to align in a more organized pattern with the flow direction, than those away from the wall. This accounts for the degradation in momentum at the walls. Also, since the die wall is impenetrable to the polymer molecules, their concentration steadily reduces to zero at the die wall (basic molecular diffusion principles), reducing the viscosity of the melt accordingly.

Three different representations and implementations for slip are considered in this present work to describe the behaviour of the polymer flow and to analyse the effects of wall slip. We identify the details of each below.

3.4.1. Navier slip law. As shown by Silliman and Scriven [15], the Navier slip law may be incorporated naturally into a variational formulation of the governing flow equations. A slip coefficient (α) for condition 1 may be adopted at the die surface prior to the die exit. The general form of boundary condition deals explicity with velocity, stress and slip respectively. The boundary condition dealing solely with velocity is satisfied through specification of the associated interpolation shape functions $\{\phi_j\}$. The natural boundary condition for stress is combined with the residual boundary terms of the Galerkin process. The slip boundary condition, also known as the Robbins boundary condition, may be embedded within such a problem statement. This is accomplished through the variational formulation, so that the integral term incorporated, dealing with the slip boundary conditions is of the form

$$\alpha \int_{\Gamma} \phi_i \mathbf{U} r \, \mathrm{d}\Gamma, \quad \alpha = \frac{\alpha_1}{\alpha_0}$$

Here, Γ is the relevant slip boundary section, r is the radial co-ordinate, and ϕ_i is the finite element residual-weighting function.

3.4.2. Phan-Thien slip rule. Phan-Thien [16] applied slip at the wall, by expressing the slip velocity as a function of wall shear stress. In this method, a steady slip velocity is imposed governed by the wall shear stress exceeding some critical value. The functional prescription imposed here is

$$U_{\text{slip}} = U_{\text{mean}} f(X), \quad U_{\text{mean}} = \frac{Q_{\text{ns}}}{\pi R^2}$$

$$f(X) = 1 - \exp(-a_0 X), \quad X = \frac{\tau}{\tau_{\text{crit}}}$$

where variables are defined as slip velocity U_{slip}, mean velocity U_{mean}, flow rate assuming no-slip boundary condition Q_{ns}, radius of channel width R, constant slip coefficient a_0, wall shear stress τ, and critical shear stress τ_{crit}.

3.4.3. Pure slip. The case of pure slip is specified through the Navier slip law, ensuring vanishing shear stress at the die wall boundary, *viz*.

$$\hat{\mathbf{t}} \cdot \hat{\mathbf{T}} = (\tilde{\boldsymbol{\sigma}} \cdot \hat{\mathbf{n}}) \cdot \hat{\mathbf{t}} = 0$$

where $\tilde{\boldsymbol{\sigma}}$ represents the Cauchy stress tensor.

4. PROBLEM SPECIFICATION

In this study we concentrate on three types of flows, a short-die pressure-tooling flow, a full pressure-tooling case and a tube-tooling flow. The first case provides a preliminary look at a model flow for pressure-tooling, without the full die complexity, concentrating on die-exit

conditions and the interface between pressure-driven shear flow and drawing flow. No-slip and various implementations of slip are applied at the die wall prior to die exit, including Navier slip law, Phan-Thien slip rule and pure slip. This permits an investigation of slip conditions and their influence on die exit flow conditions through variables such as shear rate. Also of interest is the adjustments that this causes in the free-jet drawing flow (swelling) that subsequently forms the coating upon the wire. By necessity, this implies the need for a free surface location method.

A steady slip velocity is imposed via the Phan-Thien slip. Pure slip ensures zero tangential traction to the slip boundary and the Navier slip law provides a balance of tangential traction against a frictional component expressed through the slip velocity. These latter two implementations that involve tractions are achieved in a natural boundary integral manner via the variational formulation (see Silliman and Scriven [15]). A critical value of wall shear stress is employed as a mechanism to trigger slip.

Distinction can be drawn between pressure- and tube-tooling designs, as depicted schematically in Figure 1. For tube-tooling, the upper and lower boundary zones of $Z_5Z_6Z_7$ and $Z_8Z_9Z_{10}$ are free surfaces in the draw-down and coating region. In the case of pressure-tooling, only the upper zone beyond the die is a free surface, and the coating flow (polymer melt) meets the moving wire within the die.

4.1. Short die pressure-tooling

The domain of consideration for this annular pressure-tooling flow is illustrated in Figure 1(a). For this problem, a sufficiently fine mesh was generated with 6×24 elements, 637 nodes, 1449 degrees of freedom, and minimum size of element 0.0645 units as demonstrated in Figure 2(a). This model test problem largely resembles the classical die-swell flow but with the additional consideration of an imposed drag flow from a moving lower (wire) boundary. There are two regions of different character to the flow, a shear flow within the die and a free jet drawing flow beyond. Boundary conditions are provided via an imposed inlet flow profile of fully developed pressure-driven annular flow. This setting predefines the assigned flow rate, fixing it henceforth, with no-slip conditions imposed on the die wall. Throughout all computations, the lower boundary is considered as moving at a constant specified speed. A streamline defines the location of the free jet boundary surface upon which vanishing traction applies, and the outlet flow is taken as a fully developed plug flow. The characteristic length and velocity are equivalent to the inlet channel radius, inclusive of wire radius, (or one radial unit of coating length) wire speed respectively. The associated dimensions of the domain are provided in Figure 1, where wire radius is 0.6 units.

4.2. Pressure-tooling

A schematic diagram of the full pressure-tooling flow is shown in Figure 1(b), for which the associated mesh of 12×74 elements, 3725 nodes and 8425 degrees of freedom is displayed in Figure 7(a). As above, the assigned pressure-driven annular entry flow meets the moving wire at station Z_{10} (see Figure 1(b)) inside the die. On exiting the die, there is swelling at the free boundary region Z_6Z_7. For the standard implementation involving no-slip, the boundary conditions read as follows: at the die wall of sections Z_2Z_6 and Z_1Z_{10}, no-slip applies; at the

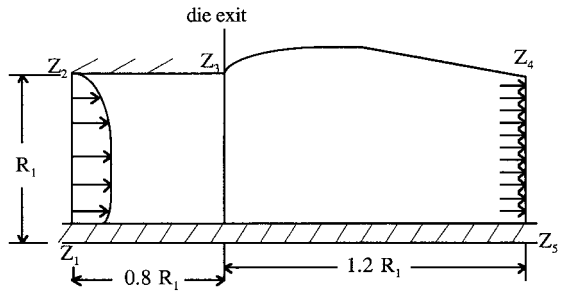

(a) **short-die pressure-tooling**

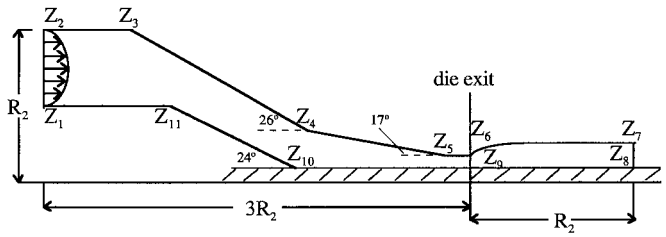

(b) **pressure-tooling**

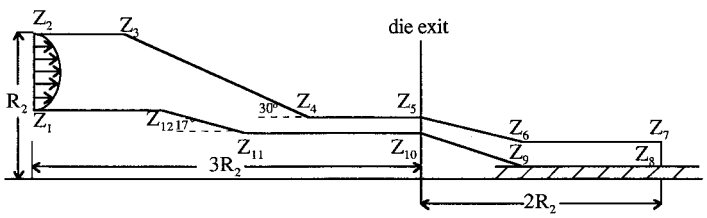

(c) **tube-tooling**

Figure 1. Schema for extrusion coating flows.

free surface section Z_6Z_7, tractions vanish and the arbitrary level of pressure is fixed; at outflow Z_7Z_8, a plug flow is imposed travelling with the moving wire. The lower domain boundary corresponding to the moving wire, Z_8Z_{10}, moves at the prescribed wire speed.

Characteristic length and velocity scales are selected as coating length R_2 and wire speed. The die length is 3 units, wire radius is 0.09 units, inlet hydraulic radius (Z_1Z_2) is 0.5 units, exit hydraulic radius (Z_7Z_8) is 0.2 units and land length Z_5Z_6 is 0.05 units. Die converging angles at locations Z_4, Z_5 and Z_{10} are 26°, 17° and 24°.

4.3. Tube-tooling

The tube-tooling flow is composed of a shearing die flow, combined with a draw-down and coating section beyond the die, as shown schematically in Figure 1(c). Figure 10(a) demonstrates the fine mesh employed for this case, comprising of 12×88 elements, 4425 nodes and 10 007 degrees of freedom.

The boundary conditions for no-slip follow largely the specification for pressure-tooling, with the exception that the sides of the draw-down section Z_5Z_6 and Z_9Z_{10}, are treated here as free surfaces. The characteristic length R_2 is taken as the coating length upon the wire (also equates to the radial distance from the inlet top die boundary wall to the centre of the wire). The characteristic velocity scale is equivalent to the wire speed. The wire dimensions, the die length and inlet hydraulic radius are all as specified above for pressure-tooling. The die converging tube has angles of 30° at Z_4 and 17° at Z_{11}.

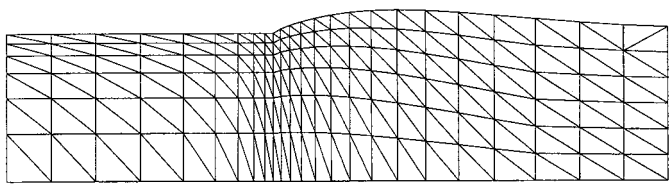

(a) **mesh pattern, 6x24 elements**

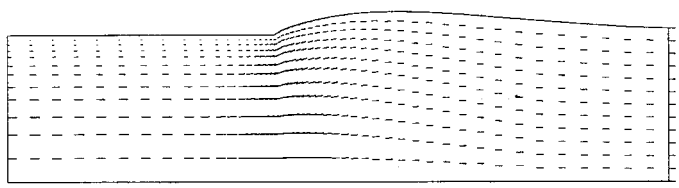

(b) **velocity vectors**

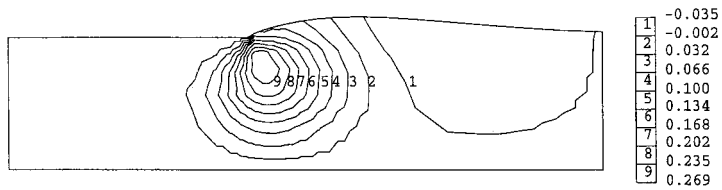

(c) $\mathbf{V}_r$ **contours**

Figure 2. Short die pressure-tooling: no-slip.

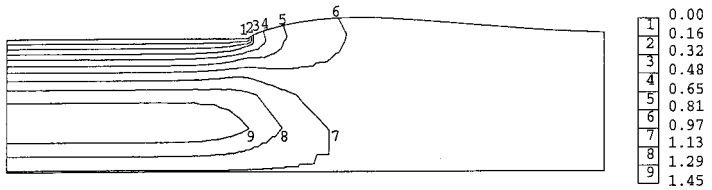

(d) $\mathbf{V}_z$ **contours**

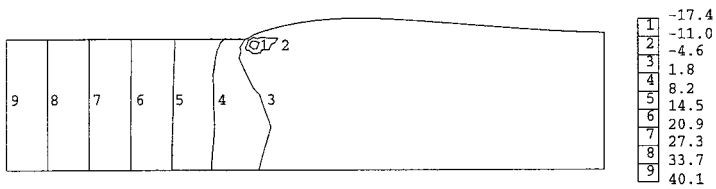

(e) **pressure contours**

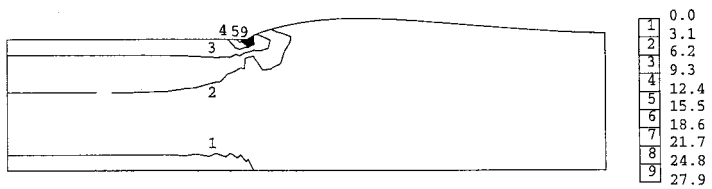

(f) I_2 **contours**

Figure 2 (*Continued*)

5. RESULTS AND DISCUSSION

Unless otherwise stated, all results pertain to Newtonian flow at minimal levels of inertia, equating to $Re = 10^{-4}$.

5.1. Short die pressure-tooling

5.1.1. No-slip conditions. The results for no-slip computations and the short die pressure-tooling flow are illustrated in Figures 2 and 3. Simulation with a 288-element mesh (Figure 2(a)) gave the velocity vectors and accompanying radial and axial velocity contour plots of Figure 2(b)–(d). The flow profiles reflect an adjustment from an initial shear flow to a plug flow, see also References [27,32]. Any die swell incurred for this type of drag flow is minimal. The shear rate contours of Figure 2(f) and the top surface line plot (see Figure 4(b)) illustrate how the

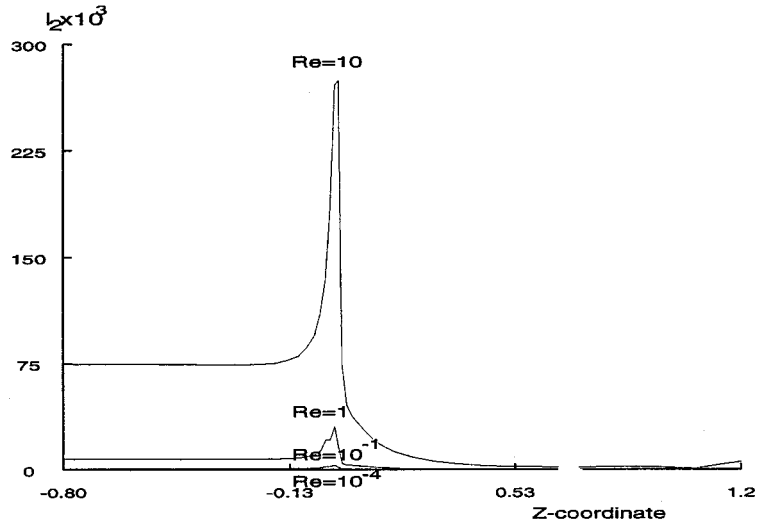

(a) I_2 **on top surface**

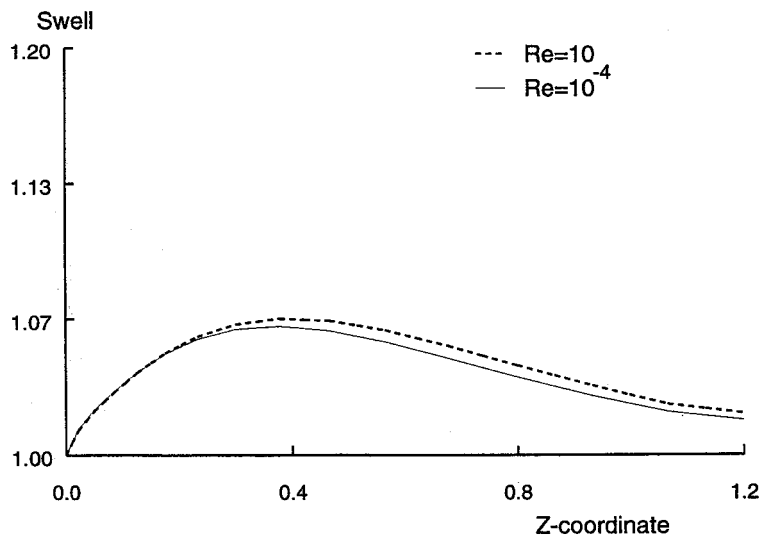

(b) **die swell**

Figure 3. Short die pressure-tooling: various Reynolds numbers, no-slip.

shear rate encounters a rapid rise near the die exit, followed by a dramatic decay immediately in the jet drawing flow. Pressure drop across of die alone is in the order of 40.1 units (Figure 2(e)), where the die is twice the length of the exit gap width. A peak pressure zone is observed near the top surface die exit point in the jet of about -17.4 units. Figure 3(a) demonstrates the effect of increasing inertia in terms of I_2, the second invariant of the rate of strain tensor, the progressive variation covering a four-decade ascension from 10^{-4} to 10. Here, inertia is increased via material properties (viscosity), while maintaining a fixed flow rate. There are only minor adjustments to the flow patterns in Figure 3(b), with slight increase of die swell at the larger value of Reynolds number (peak value of 10). This is as to be anticipated for a constant flow rate setting. Expectations would be different for comparisons based on increasing velocity scale instead.

5.1.2. Slip conditions. Slip results are recorded for each of the three slip cases instances cited in Section 4.1, of Navier slip law (NV slip), Phan-Thien slip rule (PT slip), and pure slip, to be contrasted against the foregoing no-slip case. Three choices of critical wall shear stress settings have been tested of 10.6, 11.3 and 12.3 units. The elevation of critical wall shear stress has the effect of delaying the onset of slip untill the threshold value of wall shear stress has been exceeded, drawing this initiation point closer to the die exit with increasing threshold value.

The short-die pressure tooling problem was selected as the model case upon which to conduct investigation of the various implementations of slip outlined above, prior of consideration of full tube- and pressure-tooling specifications. This lead to a parameter sensitivity analysis for the Navier slip law, considered with a critical wall shear stress τ_{crit} of 10.6 units. Simulations were performed for various slip coefficient values (α) ranging from 0 to 100, noting that vanishing α reflects pure-slip, while large α provides dominant no-slip conditions. For $\alpha = 0$, 1, 10 (Table I) there is little variation in swelling ration, $\chi =$ (jet radius)/(die exit width), and maximum slip velocity (V_{slip}) values at the die wall. The maximum deviation in χ is of order 0.4 and in V_{slip} is 30 per cent. It is noted that for $\alpha = 100$ wall slip velocity is maximized, while die swell is minimized. It is instructive to compare the results for NV slip as a function of α, against those for the case of pure slip ($\alpha = 0$). The most significant differences in χ are observed at $\alpha = 100$, with enhance slip velocity for lesser swell. At the smallest value

Table I. Short die pressure-tooling, Navier slip law for various α, $\tau_{\text{crit}} = 10.6$: velocity, shear rate, pressure, swelling ratio, and slip velocity.

α		V_r	V_z	I_2	P	χ	V_{slip}
0	Min	−0.002	0.000		−14.00		
	Max	0.220	1.453	15.25	31.40	1.012	0.901
1	Min	−0.002	0.000		−14.06		
	Max	0.221	1.453	15.28	31.38	1.012	0.903
10	Min	−0.002	0.000		−14.66		
	Max	0.226	1.453	15.28	31.19	1.011	0.919
100	Min	−0.001	0.000		−23.11		
	Max	0.296	1.453	20.06	28.58	1.008	1.175

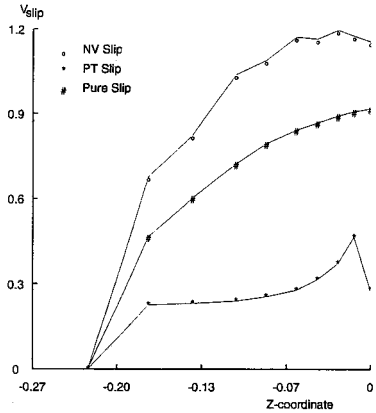

(a) **slip velocity at die wall**

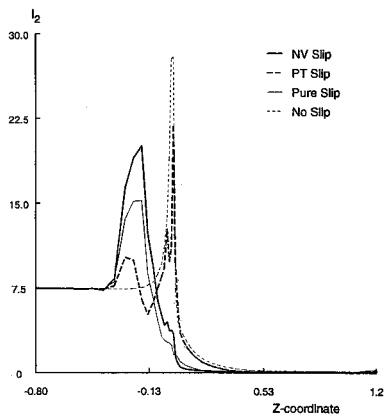

(b) I_2 **on top surface**

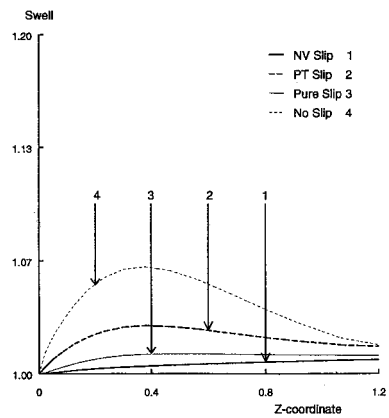

(c) **die swell**

Figure 4. Short die pressure-tooling: various slip laws, $\tau_{crit} = 0.16$.

of $\tau_{crit} = 10.6$, the short die pressure-tooling slip velocities at the upper die wall are compared for the three cases stated above (Figure 4(a)). The slip velocity behaviour can be seen to vary considerably in each case, with the NV ($\alpha = 100$) slip law reaching the highest speeds (and lowest swelling ratio), followed by pure slip and then PT slip. In all instances, the onset of slip occurs at 0.22 units distance prior to the die exit (denoting the origin).

A more detailed comparison of I_2 at the top surface, V_r, V_z, pressure, swelling ratio and the maximum slip velocity at the die wall can be found in Table II. This table also includes complete comparisons for two other critical wall shear stress settings of 11.3 and 12.3 units. Overall, maximum shear rates reduce by half and pressure drops across the flow (equating to

Table II. Short die pressure-tooling, no-slip and various slip cases: velocity, shear rate, pressure, swelling ratio, and slip velocity.

		V_r	V_z	I_2	P	χ	V_{slip}
No-slip	Min	−0.035	0.000		−17.36		
	Max	0.269	1.450	27.94	40.08	1.067	0.000
$\tau_{crit} = 10.6$							
PT slip	Min	−0.021	0.000		−10.83		
	Max	0.210	1.452	21.79	36.50	1.029	0.457
Pure slip	Min	−0.002	0.000		−13.99		
	Max	0.220	1.453	15.24	31.40	1.012	0.901
NV slip	Min	−0.001	0.000		−23.11		
	Max	0.296	1.453	20.06	28.58	1.008	1.175
$\tau_{crit} = 11.3$							
PT slip	Min	−0.024	0.000		−11.87		
	Max	0.218	1.453	22.95	37.49	1.051	0.438
Pure slip	Min	−0.009	0.000		−17.72		
	Max	0.217	1.453	18.04	34.64	1.017	0.777
NV slip	Min	−0.005	0.000		−24.02		
	Max	0.250	1.453	21.74	33.56	1.014	0.908
$\tau_{crit} = 12.3$							
PT slip	Min	−0.024	0.000		−11.12		
	Max	0.237	1.453	21.86	38.02	1.031	0.409
Pure slip	Min	−0.016	0.000		−21.77		
	Max	0.230	1.453	20.92	36.82	1.024	0.627
NV slip	Min	−0.015	0.000		−25.99		
	Max	0.234	1.453	23.25	36.48	1.022	0.689

maximum pressure values) decrease with introduction of slip. The greatest impact on pressure, swell and slip velocity is borne out through the NV slip option, here considered for $\alpha = 100$.

Figure 4(b) summarizes the behaviour of I_2 at the top flow surface for the three slip implementations at $\tau_{crit} = 10.6$ and the no-slip case. The slip instances reduce the magnitude of the discontinuity from the no-slip case by shifting upstream the stick–slip discontinuity from the die exit point, to within the die and where slipping first occurs, thus agreeing with Silliman and Scirven [15] and Phan-Thein [16]. This is confirmed via the slip velocity profile plots along the top surface in Figure 4(a). The largest jump from zero to the first non-vanishing slip velocity at the die wall occurs for NV slip, followed by the pure slip and then the PT slip cases. Hence, this is reflected in the I_2 plot of Figure 4(b), where the NV slip option generates the largest I_2 value within the die for the slip implementations. Conversely at the die exit, the most dramatic increase in I_2 value corresponds to no-slip, with NV slip and pure slip being devoid of any upward trend. These comments are valid even withstanding the difference in mesh structure for the various zones in question. The I_2 double oscillation profile, most pronounced in the PT slip case, is primarily caused by the two transitions in wall velocity, one at the stick–slip point and the other at the die exit. The elevation parameter a_0 of the PT slip rule strongly influences this second profile oscillation at the die exit. Increasing the critical wall shear stress to 11.3 and 12.3 units has the effect of shifting these transitions closer to the die

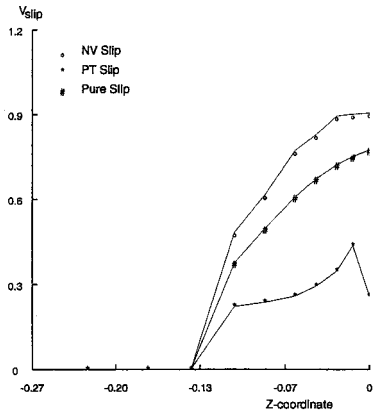

(a) **slip velocity at die wall**

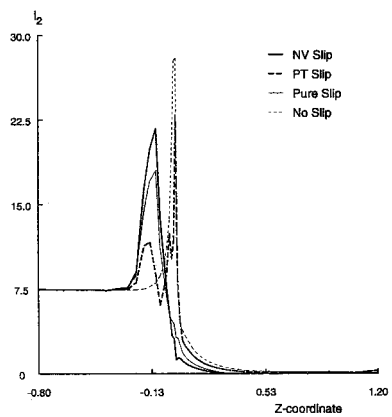

(b) I_2 **on top surface**

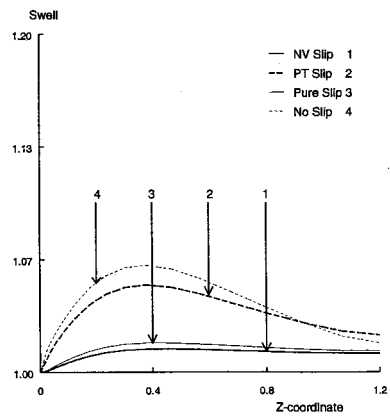

(c) **die swell**

Figure 5. Short die pressure-tooling: various slip laws, $\tau_{crit} = 11.3$.

exit (as demonstrated through Figures 5 and 6). The magnitude of die swell encountered for each of the slip and no-slip cases is shown in Figures 4(c), 5(c) and 6(c) and indicates that slip reduces swell, with NV slip giving the minimal swell. The extent of this variation in swell is of the order of 2–5 per cent of the die exit width.

At all three τ_{crit} settings tested in Table II, the shear rate (I_2) for pure slip is smaller than other slip and no-slip cases. Hence, and as a consequence, since a principal process optimization guideline is to minimize peak shear rates, further investigation focuses upon the pure slip case for the full tube an pressure tooling studies below.

5.2. *Pressure- and tube-tooling die flow analysis*

To gain some basic insight into the flow patterns and behaviour for the process conditions in question, some preliminary computations were performed on the die sections alone. This enables an assessment to be made of the extent of shear versus extension, their localization and a contrast between pressure- and tube-tooling flows. Die exit conditions are taken as fully developed flow, tantamount to assuming an infinitely long and length. For Newtonian fluids, maximum shear rates (based on I_2) quadrupled from 41.3 units for tube-tooling to 181.3 units for pressure-tooling, with a comparable increase in extension rates (based on I_3/I_2, third and

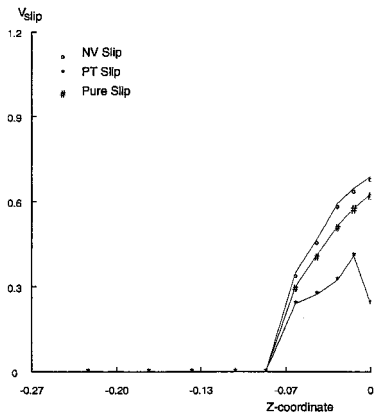

(a) **slip velocity at die wall**

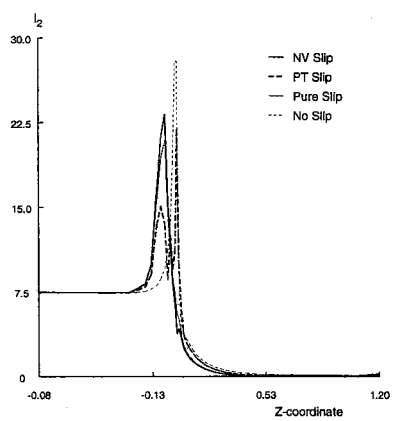

(b) I_2 **on top surface**

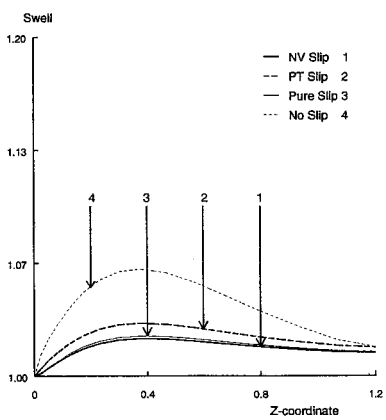

(c) **die swell**

Figure 6. Short die pressure-tooling: various slip laws, $\tau_{crit} = 12.3$.

second invariants of the rate of deformation tensor) from 5.3 to 18.7 units. Pressure drops across the die increased from 851.5 units for tube-tooling to 875.4 units for pressure-tooling. We observe below that such findings are almost entirely reproduced when full tooling cases are considered with extrudate. In contrast, for inelastic power law fluids (index 0.31), maximum shear rates triple over Newtonian values, being more closely restricted to the boundary wall region in the land section, and in particular for pressure-tooling, being more concentrated at the upper boundary die exit lip. Extension rates are barely affected by shear thinning, while pressure drop levels decrease by some three decades.

5.3. Pressure tooling

5.3.1. No-slip conditions. The no-slip pressure-tooling results are illustrated in Figure 7. The mesh of 1776 elements (Figure 7(a)) shows high levels of refinement prior to and across the land region (the 'pinched' zone of the die) and die exit regions, where detailed analysis is required. Figure 7(b)–(e) shows the velocity and contour plots. The vector plots identify flow profiles for the inlet and land zones separately, showing the gradual acceleration in the velocity flow fields. The contour plots of radial and axial velocity components illustrate the constant velocity field lines and their peak intensities. The shear rate line contours of Figure 7(g) show a peak value of 213.2 units at the die exit, with significant shearing over the land region, while this was considerably more localized in the short die case. This represents a tenfold increase in peak value of I_2 at die exit from 27.9 units for the short die case. Taking into account the difference in non-dimensionalization scales associated with each problem, in reality this increase is minimal. There is notable extension in the converging die-tube with peak extension rate of 18.7 units being located in the contraction zone, associated with the entry to the land region (Figure 7(h)). At the melt–wire contact point and in contrast to the short die case, shear rates are 10 per cent of maximum values and extension rates rise to one third of peak values. The pressure field lines of Figure 7(f) show a relatively minor pressure drop across the die, reaching a minimum of -96.3 units at the die exit. There is only minor adjustment apparent from the die-only analysis results, with an almost identical pressure drop experienced across the die, with or without the attached free jet. The profile of the shear rate I_2 at the top boundary of the die is plotted in Figure 8(b), which can be contrasted against the corresponding short-die situation of Figure 4(b). For the full pressure-tooling, there is the characteristic double peak profile, the first occurring at the beginning of the land region and the second at the die exit location. In the intermediate zone, shear rates drop to a level of 65 per cent of the peak value.

5.3.2. Slip conditions. Slip condition results are reported for the full pressure-tooling flow, utilizing the extreme of pure slip. Two values of critical wall shear stress are implemented. One value is $\tau_{\text{cirt}} = 123$ (Figure 8), for which slip applies at die wall up to and including the die exit point. For a second value of $\tau_{\text{crit}} = 135$ (Figure 9), conditions revert to no-slip at die exit. Taken in combination, this provides some insight on the interplay between the imposition of slip conditions pertaining at the die exit.

One may first look to the shear rate plots, Figure 8(b), and compare with Figure 9(b). For slip conditions and $\tau_{\text{crit}} = 135$, the peak of shear rate is doubled above the no-slip case (see Table III) at the die exit, taking up an almost identical die swell profile to that for no-slip (see

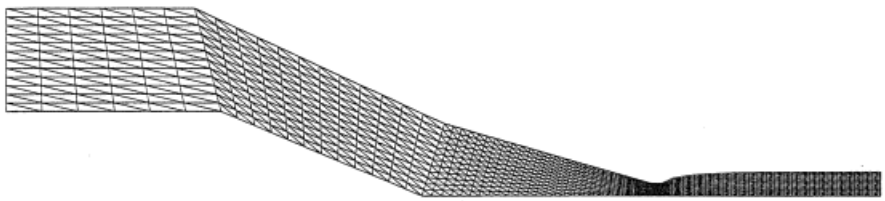

(a) mesh pattern, 12x74 elements

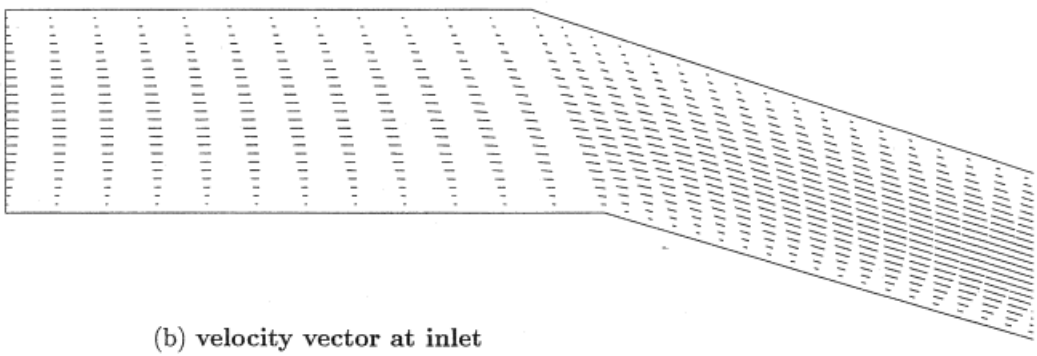

(b) velocity vector at inlet

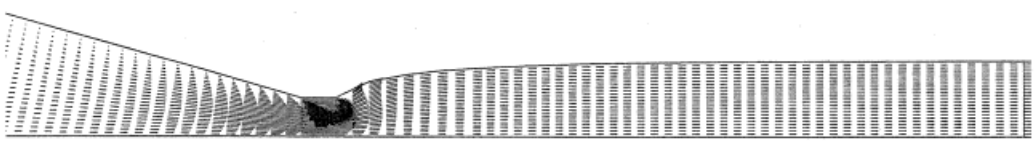

(c) velocity vector at outlet

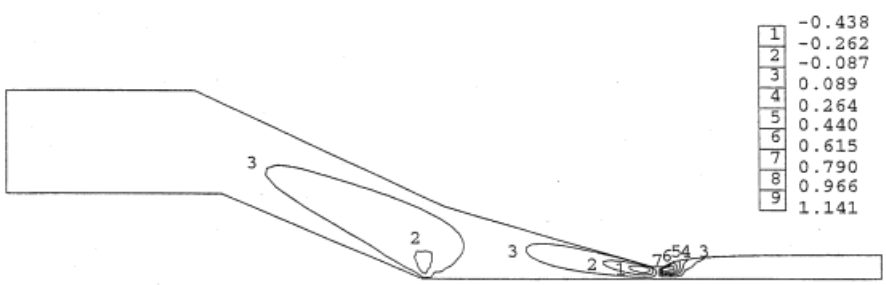

(d) V_r contours

Figure 7. Pressure-tooling: no slip.

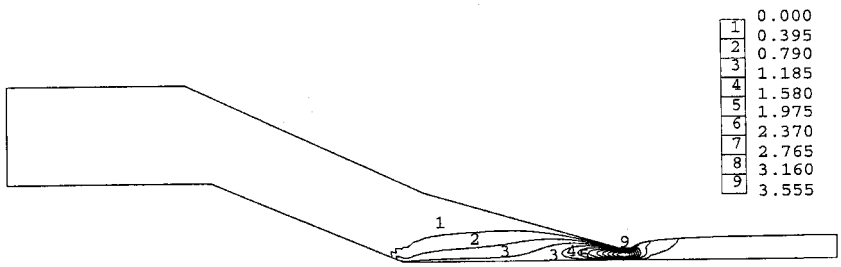

(e) $\mathbf{V}_z$ **contours**

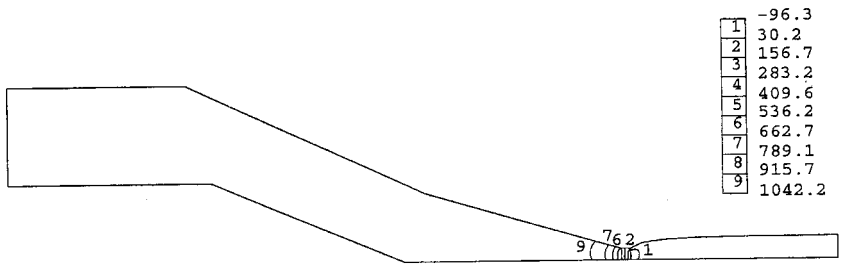

(f) **pressure contours**

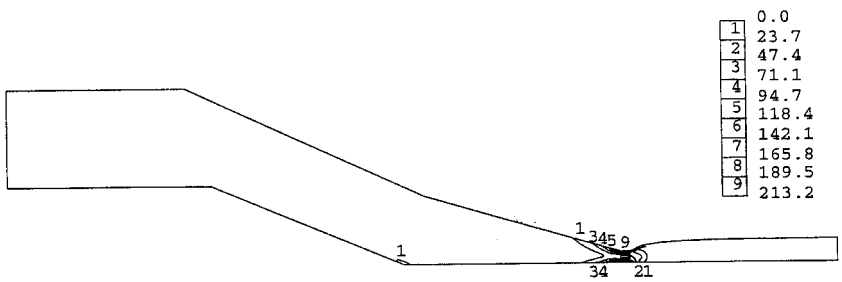

(g) I_2 **contours**

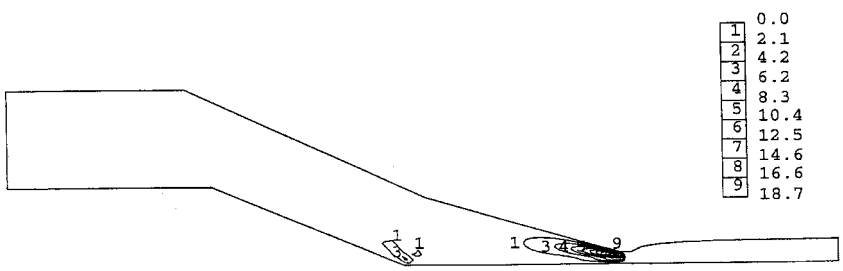

(h) **extension rate contours**

Figure 7 (*Continued*)

Figure 9(c)). The slip velocity profile is illustrated is Figure 9(a), showing the rapid decline to no-slip at the die exit.

In contrast, for slip conditions and $\tau_{crit} = 123$, peak slip shear rate reduces (by about 9 per cent) and shifts upstream of the no-slip alternative (Figure 8(b)), as in the short die problem above. A peak shear rate value of 194.7 units now occurs at the entry to the land region, and those at the die exit are significantly reduced from the no-slip scenario. The shape of the extrudate adjusts immediately after the die (Figure 8(c)), the swell is less pronounced and has a slower rate of build up than for the no-slip instance. The slip velocity profile of Figure 8(a) displays a relatively constant form up to die exit and contrasts against that of Figure 9(a).

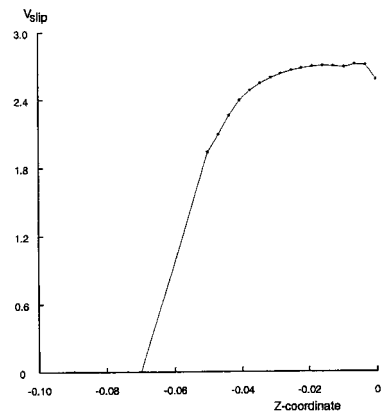

(a) **slip velocity at die wall**

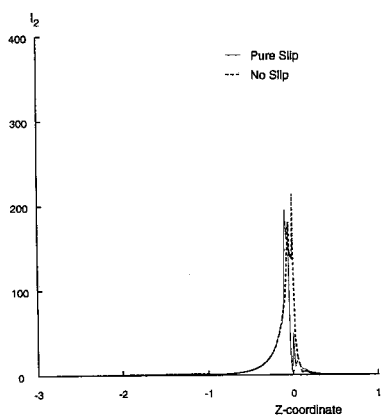

(b) I_2 **on top surface**

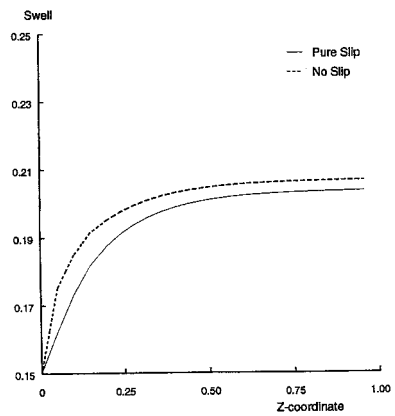

(c) **die swell**

Figure 8. Pressure-tooling: no-slip and pure slip law, $\tau_{crit} = 123$.

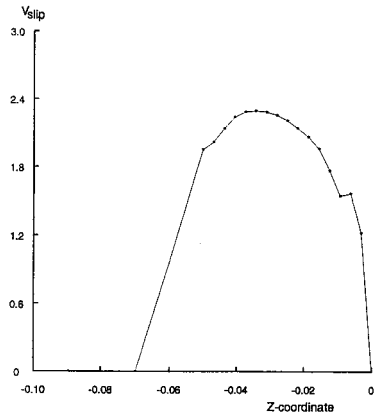

(a) **slip velocity at die wall**

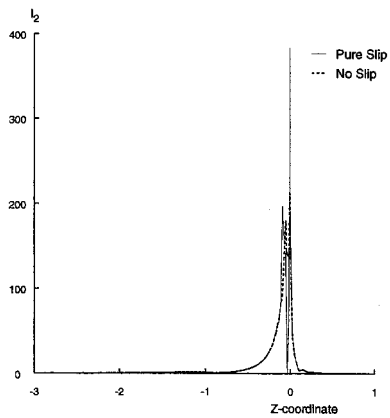

(b) I_2 **on top surface**

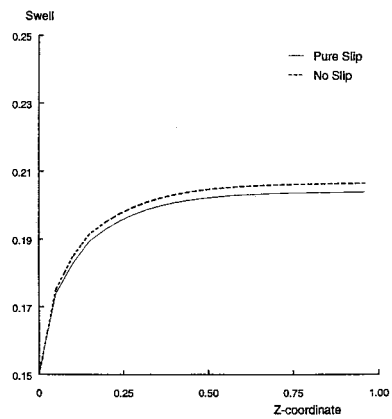

(c) **die swell**

Figure 9. Pressure-tooling: no-slip and pure slip law, $\tau_{\text{crit}} = 135$.

Extension rates barely differ between instances with or without slip. Pressure drop across the flow was noted to decrease with introduction of slip at both levels of τ_{crit}. The variation documented in Table III amounts to between 25 and 37 per cent. One concludes that for pressure-tooling and with appropriate handling of slip, reduction in shear rate at the die exit may be achieved.

Table III. Pressure tooling, no-slip conditions at two τ_{crit} values: velocity, shear rate, pressure, swelling ratio, and slip velocity.

		V_r	V_z	I_2	P	χ	V_{slip}
No-slip	Min	−0.438			−96.3		
	Max	1.141	3.555	213.2	1042.2	1.377	0.000
$\tau_{crit} = 123$	Min	−0.416			−67.4		
	Max	0.704	2.984	194.7	652.3	1.357	2.715
$\tau_{crit} = 135$	Min	−0.415			−79.9		
	Max	1.034	2.985	383.7	783.4	1.360	2.297

5.4. Tube-tooling

5.4.1. No-slip conditions. The analysis of the tube-tooling was performed with a 2112-element mesh (Figure 10(a)). This involves increasing mesh refinement approaching the angled, land and draw-down regions of the die-tube section. Close-up velocity vector profiles at the inlet and outlet of the die are supplied, as well as axial and radial components in contour form. Figure 10(b)–(e) shows the expected results and re-echo the previous descriptions for the pressure tooling case. The pressure drop of 866.7 units within the die is almost completely contained in the land section of the die (see Figure 10(f)).

A maximum shear rate of 48.6 units of observed in Figure 10(g) on the die walls within the land region. This is to be compared against 213.2 units in Figure 7(g) for pressure-tooling, some four times larger. It is noteworthy and a general observation that maximum shear rates for tube-tooling are invariably about one quarter of those encountered in the pressure-tooling flows under equitable conditions. Extension rates peak at 6.3 units at the beginning of the land region, where the flow meets the turn in the die entering the land region, which contrasts with 18.7 units in Figure 7(h) for pressure-tooling, some three times larger. Smaller, isolated local extension rate peaks are observed at the exit point on the lower boundary of the die. All these field results agree with the values obtained at the same flow rate for a die-only analysis, where a fully developed die exit flow is assumed. This would indicate that these predominant flow features within the die are not seriously affected by die exit conditions.

Figure 11(a) and (b) demonstrates the behaviour of the generalized shear rate (I_2) in profile form along both top and bottom surfaces of the flow. Here, slip and no-slip results are compared directly. For the no-slip conditions, there is a rise in value in the converging die-tube, which reaches a sustained plateau across the land region, prior to encountering a dramatic drop and levelling out in the draw-down. Both top and bottom surface profiles reflect similar form in this respect, with plateau values in the land region being about 20 per cent higher for the bottom surface. Also, the shift in peak value is seen to switch between the surface cases and the land entry and exit points. For the top surface alone and contrasting with pressure-tooling results of Figure 8(b), the essential difference in the tube-tooling design is a protracted plateau level and a reversal of peak shear rates from the exit to the entry of the land region.

5.4.2. Slip conditions. The shear rate profiles for pure slip conditions within the die, as governed by a critical wall shear stress of $\tau_{crit} = 25$ units, are included in Figure 11(a) (top surface) and (b) (bottom surface). As qualified in Table IV and in contrast to foregoing no-slip

(a) mesh pattern, 12x88 elements

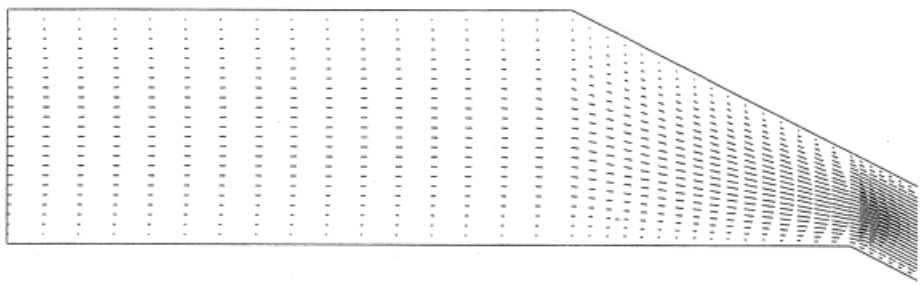

(b) velocity vector at inlet

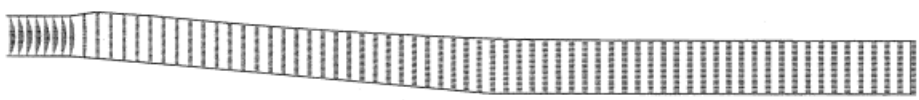

(c) velocity vector at outlet

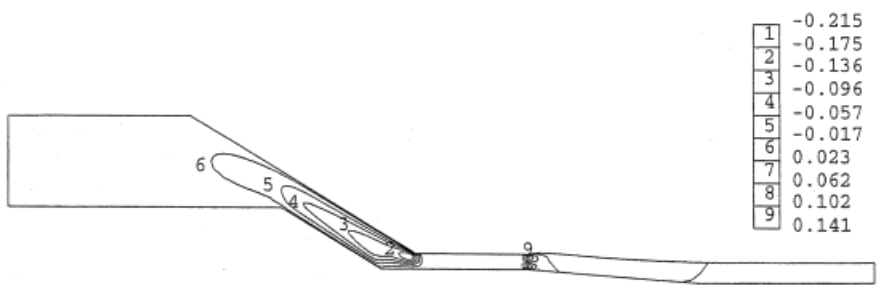

(d) V_r contours

Figure 10. Tube-tooling: no-slip.

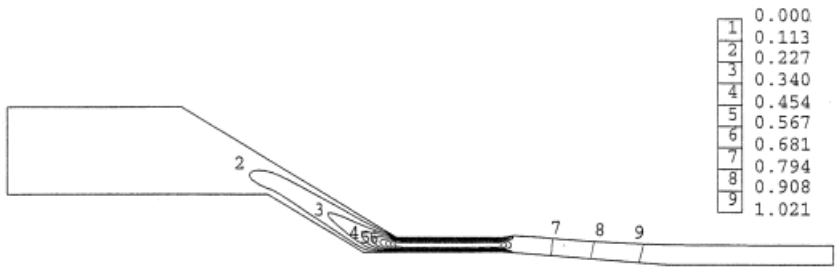

(e) V_z contours

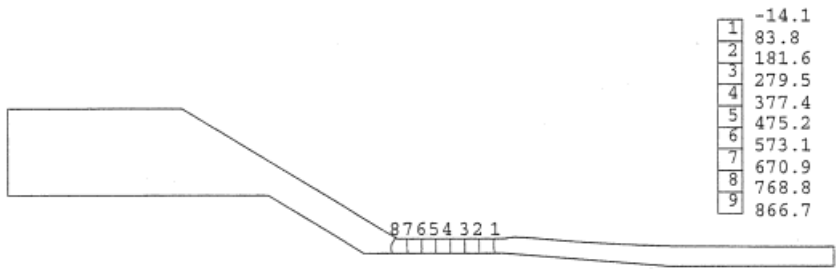

(f) pressure contours

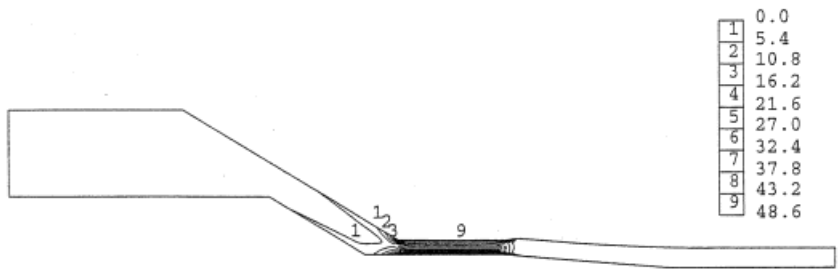

(g) I_2 contours

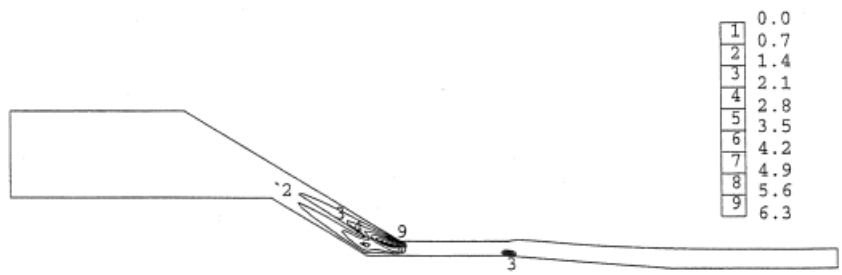

(h) extension rate contours

Figure 10 (*Continued*)

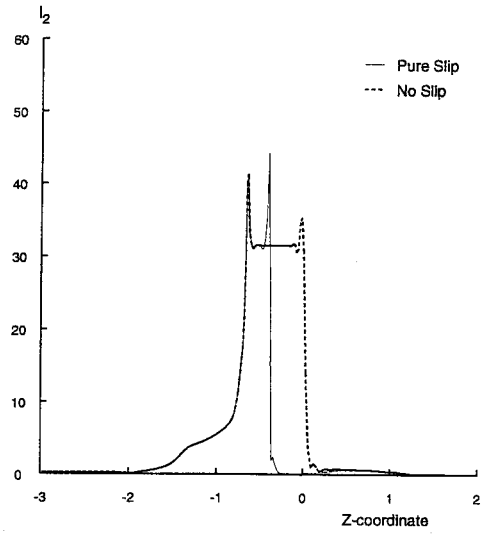

(a) I_2 **on top surface**

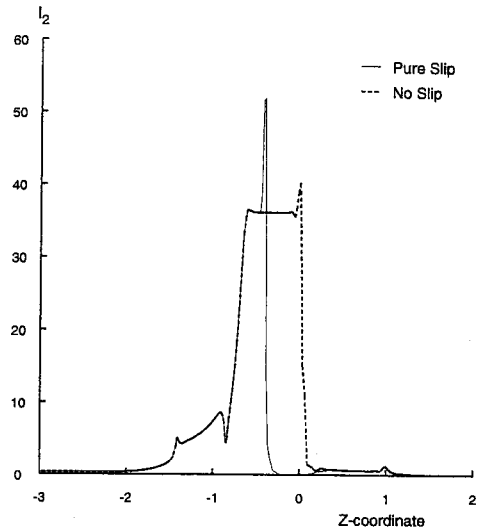

(b) I_2 **on bottom surface**

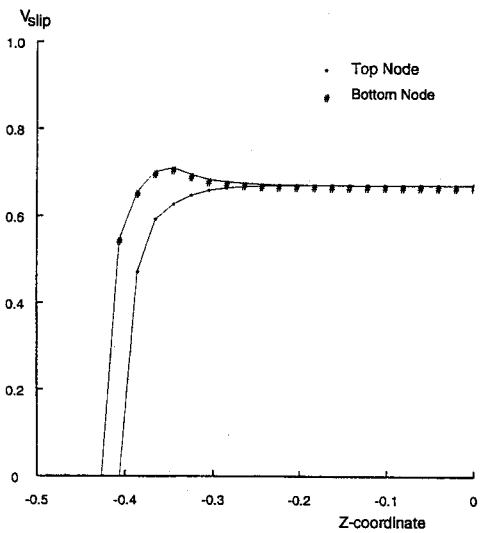

(c) **slip velocity**

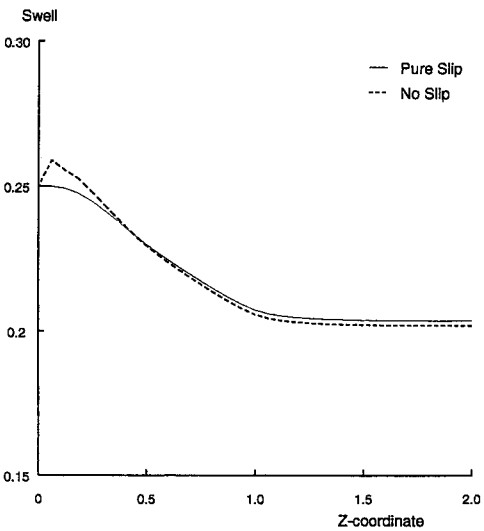

(d) **die swell**

Figure 11. Tube-tooling: no-slip and pure slip law, $\tau_{\text{crit}} = 25$.

Table IV. Tube-tooling, no-slip and pure slip conditions at τ_{crit} values: velocity, shear rate, pressure, swelling ratio, and slip velocity.

		V_r	V_z	I_2 top	I_2 bottom	P	χ	V_{slip}
No-slip	Min	−0.215	0.000			−14.11		
	Max	0.141	1.021	41.34	40.35	866.7	1.255	0.000
$\tau_{crit} = 25.0$	Min	−0.215	0.000			−30.84		
	Max	0.099	1.009	44.26	52.01	408.6	1.212	0.672
$\tau_{crit} = 29.2$	Min	−0.215	0.000			−18.37		
	Max	0.173	1.009	44.26	52.01	421.1	1.290	0.670

results, peak shear rates are larger in the land region and shifted upstream (reaching 52.01 units at the lower die wall), extension rates barely differ, and pressure drops halve (to 408.6 units). Such peak shear rates substantiate a 29 per cent increase above that for no-slip. Also, these peak values shift from the upper boundary die-wall of the land region for no-slip, to the lower wall for slip.

One feature of the top and bottom boundary shear rate profiles apparent in Figure 11(a) and (b) is that peak values at the die exit may be almost completely eliminated. However, in contrast to the pressure-tooling scenario, larger peak shear rates are stimulated upstream, within the land region, than would otherwise be the case for no-slip conditions. On the top die-surface, for no-slip the largest shear rates are observed at the turn into the land region. These are exaggerated when slip is imposed, occur downstream and provoke a 'double peak' profile. For the bottom die-surface, the largest shear rates arise at the die exit when no-slip is assumed; these are correspondingly shifted upstream and magnified when slip is introduced. The profiles of the surface slip velocities of Figure 11(c) and the free surface in Figure 11(d), for slip and no-slip conditions, are in keeping with the above observations.

Inclusion of results for a larger values of critical wall stress setting of $\tau_{crit} = 29.2$ (Table IV, Figure 12) illustrates the effect of imposing slip conditions across the land region, but reverting to no-slip at the top surface die exit. The associated shear rate profile on the top surface of Figure 12(a) picks out the second discontinuity in velocity gradient at the die exit lip, though the shear rate peak there is lower than that observed at the entry to the land region. Shear rate profiles on the lower die wall, extension and pressure fields, and slip velocity at the top surface do not vary appreciably from those for the former τ_{crit} setting. A slightly larger pressure drop of 421.1 units and swelling ratio is noted.

6. CONCLUSIONS

Through our analysis of pressure-tooling and tube-tooling coating flows, contrasting each of the tooling scenarios, along with slip and no-slip conditions, we arrive at the following general conclusions. For short die pressure-tooling, elevation of critical wall shear stress delays the onset of slip to an initiation point closer to the die exit with increasing threshold value. Maximum shear rates reduce by half and pressure drops decrease upon introduction of slip.

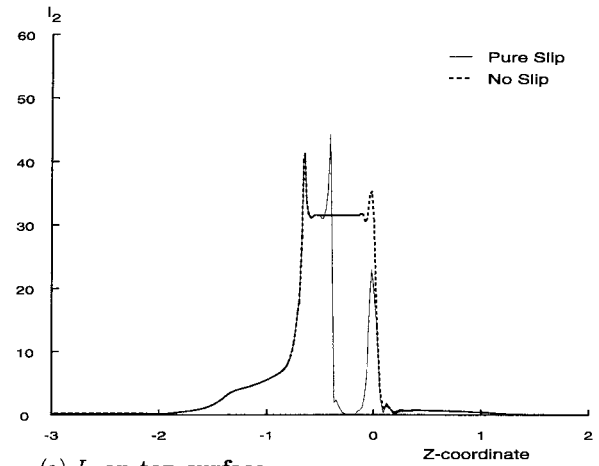

(a) I_2 **on top surface**

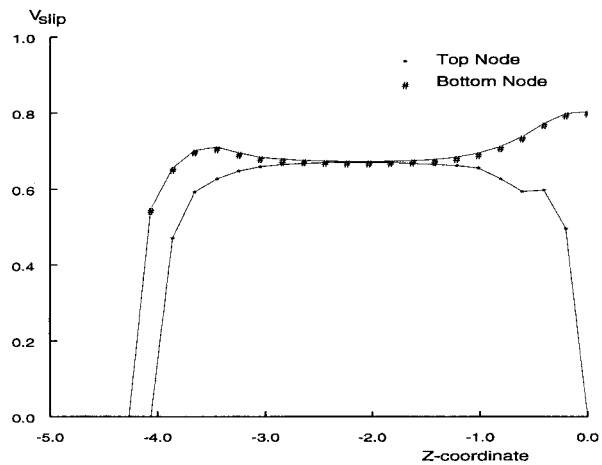

(b) **slip velocity**

Figure 12. Tube-tooling: no-slip and pure slip law, $\tau_{crit} = 29.2$.

The greatest impact on pressure, swell and slip velocity is borne out through the Navier slip law option. In contrast to pure slip ($\alpha = 0$), the most significant differences in die swell are observed for NV slip and $\alpha = 100$ with enhanced slip velocity for lesser swell. The inclusion of slip reduces the magnitude of the stick–slip discontinuity from the no-slip case, shifting this upstream from the die exit point.

Analysing the full pressure-tooling flow, there is the characteristic double peak profile in shear rate, the first occuring at the land entry (absent for the short-die) and the second larger peak at the die exit. For slip conditions right up to die exit with $\tau_{crit} = 123$, peak shear rate reduces and shifts upstream of that for no-slip. A peak shear rate occurs at the entry to the

land region, and those at the die exit are significantly reduced from the no-slip scenario. The shape of the extrudate adjusts immediately after the die, the swell is less pronounced and has a slower rate of build up than that for the no-slip alternative. For slip conditions and $\tau_{crit} = 135$, which revert to no-slip conditions at the die exit, the peak of shear rate is doubled there above that for no-slip and then, die-swell reflects no-slip findings. One concludes that for pressure-tooling and with appropriate handling of slip, reduction in shear rate at the die exit may be achieved.

In contrasting full tube-tooling against equivalent pressure-tooling flows, it is apparent that maximum shear rates for tube-tooling occur on the die walls within the land region and are about one quarter of those encountered in pressure-tooling. Extension rates peak at land entry, where the flow meets the turn in the die entering the land region, with tube-tooling values being one third of those observed for pressure-tooling. For the top surface alone and contrasting with the pressure-tooling results, the essential difference in the tube-tooling design is a protracted plateau level and a reversal of peak shear rates from the exit to the entry of the land region.

Considering slip for tube-tooling, peak shear rates shift from the upper boundary die-wall of the land region for no-slip, to the lower wall for the case with slip and increase by one-third in value. Such peak at die exit may be almost completely eliminated with slip. Nevertheless, in contrast to the pressure-tooling scenario, larger peak shear rates are stimulated upstream within the land region, than would otherwise be the case for no-slip conditions. Reverting to no-slip at the top surface in the neighbourhood of the die exit, picks out the second discontinuity in the associated shear rate profile at the die exit lip, that is characteristic of no-slip. This second discontinuity is lesser in value than that corresponding to the land entry.

The present study has ignored elastic effects as a first approximation. It is recognized that extrudate swell will be limited thereby and that shifting to a viscoelastic framework may well prove a more severe context demanding yet further considerations.

REFERENCES

1. Hawken DM, Tamaddon-Jahromi HR, Townsend P, Webster MF. A Taylor–Galerkin based algorithm for viscous incompressible flow. *International Journal for Numerical Methods in Fluids* 1990; **10**: 327–351.
2. Ding D, Townsend P, Wenster MF. Finite element simulation of an injection moulding process. *International Journal for Numerical Methods in Heat and Fluid Flow* 1997; **7**(7): 751–766.
3. Nadiri F, Fenner RT. Performance of extrusion crossheads in multilayer cable covering. *Polymer Engineering Science* 1980; **20**(5): 357–363.
4. Mitsoulis E. Finite element analysis of wire coating. *Polymer Engineering Science* 1986; **26**(2): 171–186.
5. Mitsoulis E, Wagner R, Heng FL. Numerical simulation of wire-coating low-density polyethylene: theory and experiments. *Polymer Engineering Science* 1988; **28**(5): 291–310.
6. Han CD, Rao D. Studies on wire coating extrusion. I. The rheology of wire coating extrusion. *Polymer Engineering Science* 1978; **18**(13): 1019–1029.
7. Mutlu I, Townsend P, Webster MF. Simulation of cable-coating viscoelastic flows with coupled and decoupled schemes. *Journal of Non-Newtonian Fluid Mechanics* 1998; **74**: 1–23.
8. Caswell B, Tanner RI. Wire coating die design using finite element methods. *Polymer Engineering Science* 1978; **18**(5): 416–421.
9. Mutlu I, Townsend P, Webster MF. Computation of viscoelastic cable coating flows. *International Journal for Numerical Methods in Fluids* 1998; **26**: 697–712.
10. Kasajima M, Ito K. *Applied Polymers Symposium* 1972; 221.
11. Paton JB, Squire PH, Darnell WH, Cash FM, Carley JF. In *Processing of Thermoplastic Materials*, Bernhardt EC (ed.). Reinhold: New York, 1959; 269–299.

12. Mckelvey JM. *Polymer Processing*. Reinhold: New York, 1962.
13. Hatzikiriakos SG, Dealy JM. Role of slip and fracture in the oscillating flow of HDPE in a capillary. *Journal of Rheology* 1992; **36**(5): 845–884.
14. Ramamurthy AV. Wall slip in viscous fluids and influence of materials of construction. *Journal of Rheology* 1986; **30**: 337–357.
15. Silliman WJ, Scriven LE. Separating flow near a static contact line: slip at a wall and shape of a free surface. *Journal of Computational Physics* 1980; **34**: 287–313.
16. Phan-Thien N. Influence of wall slip on extrudate swell: a boundary element investigation. *Journal of Non-Newtonian Fluid Mechanics* 1988; **26**: 327–340.
17. Den Doelder CFJ, Koopmans RJ, Molenaar J, Van de Ven AAF. Comparing the wall slip and the constitutive approach for modelling spurt instabilities in polymer melt flows. *Journal of Non-Newtonian Fluid Mechanics* 1998; **75**: 25–41.
18. Binding DM, Blythe AR, Gunter S, Mosquera AA, Townsend P, Webster MF. Modelling polymer melt flows in wire coating processes. *Journal of Non-Newtonian Fluid Mechanics* 1996; **64**: 191–209.
19. Gunter S, Townsend P, Webster MF. The simulation of some model viscoelastic extensional flows. *International Journal for Numerical Methods in Fluids* 1996; **23**: 691–710.
20. Matallah H, Townsend P, Webster MF. Multi-mode viscoelastic simulation of cable-coating flow. Report 5-97, Department of Computer Science, University of Wales Swansea, 1997.
21. Bathe KJ, Khoshgoftaar MR. Finite element free surface seepage analysis without mesh iteration. *International Journal for Numerical Methods in Geomechanics* 1972; **3**: 13–22.
22. Omodei BJ. Computer solutions of a plane Newtonian jet with surface tension. *Computer in Fluids* 1979; **7**: 79–96.
23. Ruschak KJ. A method for incorporating free boundaries with surface tension in finite element fluid flow simulators. *International Journal for Numerical Methods in Engineering* 1980; **15**: 639–648.
24. Saito H, Scriven LE. Study of coating flow by the finite element method. *Journal of Computational Physics* 1982; **42**: 53–76.
25. Ettouney HM, Brown RA. Finite element methods for steady solidification problems. *Journal of Computational Physics* 1983; **49**: 118–150.
26. Kistler SF, Scriven LE. Coating flow theory by finite element and asymptotic analysis of the Navier–Stokes system. *International Journal for Numerical Methods in Fluids* 1984; **4**: 207–229.
27. Ngamaramvaranggul V, Webster MF. Computation of free surface flow with a Taylor–Galerkin/pressure–correction algorithm. *International Journal for Numerical Methods in Fluids* 2000; **33**: 993–1026.
28. Jiang TQ, Young AC, Metzer AB. The rheological characterization of HPG gels: measurement of slip velocity in capillary tubes. *Rheology Acta* 1986; **25**(4): 397–404.
29. Brunn P. The effect of a solid wall for the flow of dilute macromolecular solution. *Rheology Acta* 1976; **15**: 23–29.
30. Aubert JH, Tirrell M. Macromolecules in nonhomogeneous velcoity gradient fields. *Journal of Chemistry and Physics* 1980; **72**(4): 2694–2701.
31. Goh CJ, Athinson JD, Phan-Thien N. The flow of dilute polymer solution in a narrow channel. I. The slip effect in simple shear flow. *Journal of Chemistry and Physics* 1985; **82**(2): 988–995.
32. Richardson S. A stick–slip problem related to the motion of a free jet at low Reynolds numbers. *Proceeding of the Cambridge Philosophical Society* 1970; **67**: 477–489.

